Aeroelastic Shape Control Using Fiber-Optic-Measured Strain Data and Multiple Control Surfaces

Michael Simbuerger* and Daniella E. Raveh†
Technion–Israel Institute of Technology, 3200003 Haifa, Israel
and
Moshe Tur‡
Tel-Aviv University, 6997801 Ramat-Aviv, Israel

https://doi.org/10.2514/1.C036626

The paper presents an experimental study of aeroelastic shape sensing and control based on strain data measured in fiber-optic sensors (FOSs). Past studies demonstrated how FOS strain data could be used to reconstruct the static and dynamic deformed shapes of a flexible wing. The current study further develops these capabilities and demonstrates wing shape control. Specifically, FOS-measured strain data are used in an optimization scheme, with a target of keeping the wing's elastic deformations small, below a user-defined threshold, while maintaining a constant lift value (as required for trimmed flight) and with minimal usage of the control surfaces. The method is demonstrated computationally and experimentally on a wing model with four control surfaces. The wing was designed for this study, fabricated using additive manufacturing, and wind-tunnel tested. The trim optimization is performed both computationally and experimentally, following the same procedures but using strain and strain-modes data from finite element analysis and experiments. The wind-tunnel study demonstrated how a flexible wing's shape could be controlled based on experimental strain data only, without resorting to a computational model. In both the computational and experimental parts of the study, considerable control-surface deformations were required. This primarily indicates that large control surfaces are not the optimal means for wing shape control. However, the same strain-based technique can be used with other effectors, such as distributed control surfaces, strain actuators, etcetera. The study opens a path to using FOSs to optimize winged unmanned-aerial-vehicle performance, and thus design lighter and more efficient platforms.

I. Introduction

THE main goals in current aircraft design are fuel consumption and emission reduction together with improvement in performance. These can be achieved straightforwardly with lightweight aircraft. However, lightweight aircraft are inherently more flexible and susceptible to adverse aeroelastic phenomena such as flutter, reduced control-surface effectiveness, increased maneuver loads, and large dynamic response to atmospheric turbulence. This is the case for transport aircraft, fighter, or winged unmanned aerial vehicles. The traditional approach for resolving aeroelastic issues is to stiffen the structure. This, however, comes at the expense of structural weight and, ultimately, the system performance is penalized due to weight or through a reduced flight envelope. Over the years, and with advances in aircraft control technologies, several studies have shown that a flexible-winged vehicle can be controlled to achieve optimal performance while minimizing adverse aeroelastic effects. Optimal performance may be increased maneuverability (higher roll rates [1]), minimal wing root-bending moments [2], minimum drag [3–6], or limited deformations [7,8]. Although most of these designs were demonstrated numerically, maturation of technologies requires demonstration in wind-tunnel tests and on flying platforms. The current study aims at computational and experimental investigation of aeroelastic shape control for optimal performance. In that, it adds to the literature on experimental wing shape optimization with wind-tunnel hardware in the loop, introducing the use of fiber-optic strain data [9,10].

Studies on aeroelastic shape control rely on some measurement of the deflected shape. This could be, for example, wingtip displacement [7] or deformation in modal coordinates [8,11]. The former can be obtained from accelerometer measurements (and time integration), but this sort of data is noisy, local, and limited to a few points. Recent studies have shown that a detailed deformed shape of a structure could be obtained from strain data measured in optical fibers [12–14].

Fiber-optic sensing is used in the fields of civil engineering, aerospace, marine, oil, and gas. A prominent use of fiber-optic sensors (FOSs) in the aerospace industry is for structural health monitoring of complex aerostructures. FOS inherent capabilities include strain accuracy comparable with that of standard electrical strain gauges [15], spatial resolution (less than 1 cm), high sensitivity, wide strain dynamic range, high speed (in kilohertz for point sensing and tens to hundreds of hertz for distributed sensing), multiplexed operation (one fiber can support many sensors along its length), insensitivity to electromagnetic radiation, small size, and light weight. These properties, as well as suitability to be embedded into composite aerostructures without affecting their performance, make FOSs highly suitable for aerospace systems. Recent studies demonstrated the experimental use of FOSs for measurement of a flexible wing's deformed shape [14] and aeroelastic dynamic characteristics [16]. Another recent study [11] presented virtual deformation control based on FOS data. The latter study, however, was computational (namely, the strain data were simulated).

In the current study, we put these recent advancements together and test them computationally and experimentally in a wind-tunnel study of the shape control of a flexible wing. The goal of this research study is to demonstrate (first computationally and then experimentally) that wing deformations can be extracted from strain data measured in FOSs and used to control the wing shape to achieve a desired shape. In the case of the current study, we attempt to keep the wing elastic deformations under a certain threshold while maintaining a required lift force (as would be necessary for trimmed flight) and while using minimal control-surface deflections for this exercise.

For this goal, a flexible-wing wind-tunnel model was designed, analyzed, and manufactured. The wing was fitted with four trailing-edge flaps that were used to control the deformed shape. The wing

Received 1 August 2021; revision received 29 April 2022; accepted for publication 10 May 2022; published online 29 June 2022.

*Graduate Student, Faculty of Aerospace Engineering.
†Professor, Faculty of Aerospace Engineering; daniella@technion.ac.il. Associate Fellow AIAA.
‡Professor, School of Electrical Engineering.

structure was modeled using a finite element (FE) model, and its aeroelastic deformation and lift were analyzed under various flow conditions. A trim optimization study was performed to compute the expected trim flap deflections.

The wing was then studied experimentally in the subsonic wind tunnel at the Faculty of Aerospace Engineering of Technion–Israel Institute of Technology. To measure the elastic deformation, the wing was fitted with strain-measuring fiber Bragg grating (FBG) imprinted in polyimide-coated single-mode optical fibers. Other measurement devices included a motion recovery system (MRS) of three cameras that tracked infrared (IR) reflectors, as well as an inertial measurement unit (IMU) placed at the wingtip. Measured strain data from the FOS were used to compute the deformed shape (based on the algorithm and setup that were recently proposed in Ref. [14]). Sensitivities of the generalized displacements and aerodynamic coefficients to the flap deflection were estimated and used in the trim optimization. The deformed shape was compared to the computed deformed shape and to the deformed shape as measured by reference measurement devices. The paper presents the wing design, analyses, and computational and experimental shape optimization.

II. Trim Optimization for Constrained Deformations

In the current study, trim optimization is used to compute the control-surface deflections that are required to attain some lift force value (as in a trimmed flight) while constraining the elastic-wing deformations to a maximal user-defined value and while accounting for other constraints. A similar trim optimization exercise was proposed in Ref. [8]. The derivation of the static aeroelastic equations and the setup of the trim optimization problem are briefly repeated here.

A. Static Aeroelastic Model

The static aeroelastic equation of motion of a clamped wing in physical coordinates is

$$[K - q_\infty \mathrm{AIC}]\{u\} = [P_{ae}]\{\delta\} \tag{1}$$

where $[K]$ is the structural stiffness matrix, q_∞ is the dynamic pressure, [AIC] is the aerodynamic influence coefficients matrix, $\{u\}$ is the vector of nodal displacements, and $[P_{ae}]$ is a matrix of rigid aerodynamic force coefficients associated with the trim parameters $\{\delta\}$. The trim parameters include the angle of attack (AOA) α and multiple control-surface deflections δ_j.

Using the modal approach, the deformations in the discrete degrees of freedom (DOFs) are expressed as a linear combination of a subset of the wing elastic vibration modes:

$$\{u\} = [\phi]\{\xi\} \tag{2}$$

Rewriting Eq. (1) in modal coordinates, and premultiplying the equation by $[\phi_e^T]$, the modal elastic deformation can be computed as

$$\{\xi\} = [K_{ee} - q_\infty Q_{ee}]^{-1}[\phi_e]^T[P_{ae}]\{\delta\} \tag{3}$$

where

$$[K_{ee}] = [\phi_e]^T[K][\phi_e], \qquad [Q_{ee}] = [\phi_e]^T[\mathrm{AICS}][\phi_e] \tag{4}$$

In the current study, the modal elastic deformation of the first wing-bending mode, as computed from Eq. (3), is used as a constraint in the trim optimization described in the following.

B. Trim Optimization Problem Definition

In the case of a free-flying aircraft, the trim optimization problem can be defined as trimming the aircraft to a specific user-defined maneuver load factor using the angle of attack and multiple control surfaces while constraining the wing deformations [8]. In the case of the wind-tunnel clamped wing, we use trim optimization to constrain the elastic deformations while requiring some value of lift coefficient (which is the equivalent of the load factor in the free aircraft case). The angle of attack is kept fixed, and the trim variables are the n_δ control-surface deflections.

The overall wing deformation can be decreased by controlling the deformation in modal coordinates rather than by controlling the wingtip displacement. Here, we control the first-bending-mode coordinate ξ_1, which can be expressed as a function of the trim variables δ_i as

$$\begin{aligned}\xi_1 &= \xi_{1_0} + \frac{\partial \xi_1}{\partial \delta_1}\cdot\delta_1 + \ \ldots\ + \frac{\partial \xi_1}{\partial \delta_{n_\delta}}\cdot\delta_{n_\delta} \\ &= \xi_{1_0} + e_1\cdot\delta_1 + \ \ldots\ + e_n\cdot\delta_{n_\delta}\end{aligned} \tag{5}$$

where ξ_{1_0} is the wing bending due to the AOA (which is fixed in this study), without control-surface deflection, and $e_i = (\partial\xi_1/\partial\delta_i)$ are the sensitivities of the bending generalized coordinate to a unit displacement of each of the n_δ trim variables. In the general case, constraining the first bending-mode coordinate is not the same as constraining the wingtip displacement. A more flexible wing, for example, might require consideration of higher modes. For the wing under investigation, controlling the wing deformation is equivalent to controlling the first-bending-mode coordinate ξ_1, as shown in the results.

Minimizing the wing deformation (in absolute value) can be defined as the objective function for the trim optimization. However, this poses a problem: Optimization algorithms will compete for smaller values of the objective function. This may result in very small deformations, which are not necessarily required, while paying the price for using nearly all of the control surfaces at their maximum allowable values. This is not an ideal solution because it does not leave control-surface margins for further maneuvers required in flight and for gust response alleviation.

Therefore, the optimization objective is defined as minimization of the control effort while setting a maximum allowable modal deformation as a constraint. Because large negative modal coordinates are as detrimental as large positive values, we use the absolute value of ξ_1 as the constraint in the optimization.

The control effort is defined as a weighted sum of the trim parameters (control-surface deflection δ_j), in which the weight d_j represents the cost of using each control surface. In this way, it is possible to impose less usage of a certain control surface (for example, on the outboard aileron if it is reserved for maneuvering). We note that this definition of the control effort (as the weighted sum of control usage) is different from the definition in other trim optimization studies in which the control effort referred to the energy required for control-surface actuation [17,18].

The trim optimization problem is stated as

$$\begin{array}{lll}
\text{Minimize} & \beta = \sum_j (d_j\delta_j)^2 & \text{Control effort} \\
\text{subject to} & |\xi_1| \le \xi_1^{\max} & \text{Maximum deflection} \\
 & C_L = C_L^{\mathrm{req}} & \text{Trim requirements} \\
 & \delta_j^{\min} \le \delta_j \le \delta_j^{\max}\ \forall\ j & \text{Trim variable bounds} \\
 & HM_j^{\min} \le HM_j \le HM_j^{\max}\ \forall\ j & \text{Hinge moment bounds}
\end{array} \tag{6}$$

The trim requirement could represent an equilibrium of forces in a maneuver, where C_L^{req} is the required maneuver lift. Additional constraints are set on the travel range of the control surfaces (trim variable bounds) and on the allowable control-surface hinge moments HM_j (hinge moment bounds).

The optimization objective, which is minimization of control effort, is a quadratic, nonlinear function of the control-surface deflections. The optimization problem was solved in MATLAB by quadprog.m quadratic programming (for multivariable constraint quadratic optimization with linear boundary conditions) using the interior-point-convex algorithm.

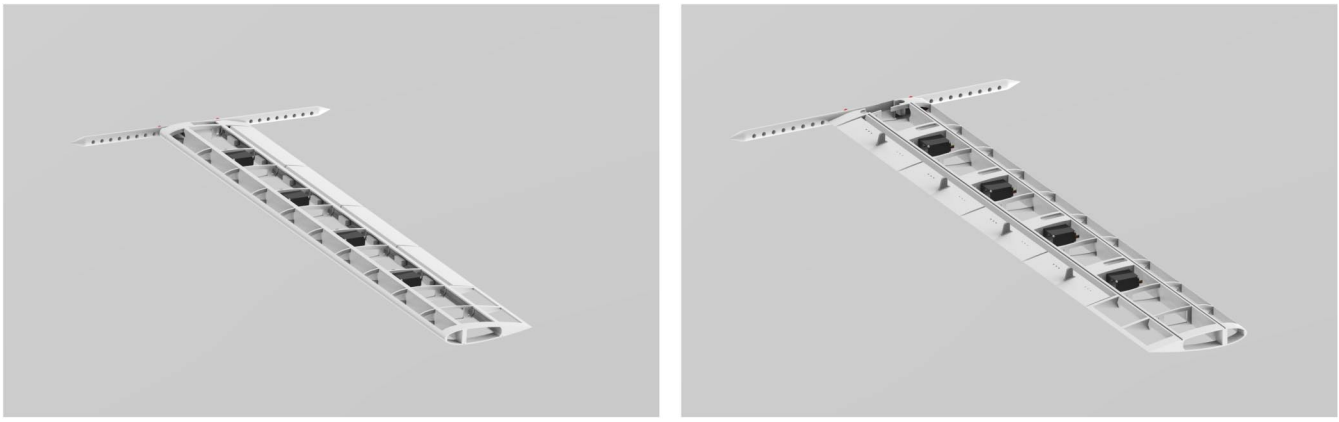

a) b)

Fig. 1 CAD rendering of the wing investigated; a) top and b) bottom sides.

C. Modal Coordinate Values from Strain Data

The novelty in the use of FOS strain data is that it allows for almost direct extraction of the modal coordinates, which are required for the optimization. There are several ways to convert strain data to deformations (see a review of such methods in Ref. [13]). The approach taken here is a modal approach that was proposed by Foss and Haugse [19] and successfully used in an aeroelastic wind-tunnel study by Freydin et al. [14]. It is briefly reviewed in the following.

The structural displacements in the discrete DOFs $\{u\}$ can be written as a combination of displacement modes of the structure as expressed in Eq. (2). Similarly, the axial strains along the span of a wing can be approximated as a combination of strain modes

$$\{\varepsilon\} = [\Psi]\{\xi\} \tag{7}$$

where $[\Psi]$ is the matrix of strain modes. The modal coordinates can be computed from measured strains by least squares as

$$\{\xi\} = [[\Psi]^T[\Psi]]^{-1}[\Psi]^T\{\epsilon\} \tag{8}$$

The strain modes required for the transformation can be computed in the same free-vibration analysis that is used to calculate the displacement modes. The exact computational procedure is detailed in Ref. [14]. Alternatively, the strain modes can be extracted from a ground-vibration test (GVT) in which strains are measured. The current study performs the trim optimization twice: once computationally, and once experimentally. Strain modes from FEs are used in the computational optimization; and measured strain modes, from GVT, are used in the experimental case. The latter have the advantage that they are completely independent of a FE model. All the required data for strain to displacement mapping (namely, the displacement and strain modes) are extracted experimentally in the GVT. A comparison of results extracted from either mode set is also presented.

III. Wing Design and Analyses

The methodology is implemented and tested on a wing model in the wind tunnel. The wing was designed by considering the wind-tunnel constraints: a wind-tunnel section of 1×1 m and wind-tunnel speeds up to 100 m/s. Figure 1 shows the wing CAD model. The wingspan is 600 mm, and the wing chord is 100 mm. The wing section is a NACA 0018. Four trailing-edge control surfaces span the rear 30% of the chord. A loading beam of 10 mm in diameter at the wingtip extends ahead of the leading edge (LE) and behind the trailing edge (TE). The loading beam is used to add concentrated weights to modify the wing's inertial properties and flutter onset speed.

The wing was designed and manufactured using rapid prototyping in Nylon-12 material. The nominal material properties (as provided in the material's data sheet) are a Young's modulus of $E = 1.65$ GPa, a Poisson's ratio of $\nu = 0.33$, and a density of 986.6 kg/m^3. For the aerodynamic shape, the wing was wrapped in polyester foil that is typically used for radio-controlled models. The Young's modulus of the foil was estimated from a tensile test as $E = 1.83$ GPa [20]. The weight of the foil was negligible. These Nylon-12 and polyester material properties were used for the wing design. They were then adjusted in the FE model to adapt it to static loading and GVT results, as presented in Sec. III.A.

Four control surfaces are connected to the rear spar via hinges, and they are deflected using servos. Each servo is mounted between two spars in an L-shaped reinforcement plate (which is also three-dimensionally printed as part of the wing). Overall, with the control-surface servos and the instrumentation, the wing weighs 0.283 kg.

On one side of the wing, two optical fibers were embedded in cavities in the main and rear spars (Fig. 2), with each containing 15 equally spaced FBG strain sensors. The fibers were glued to the wing using epoxy resin.

A. Structural Finite Element Model

The wing structure was modeled in NX NASTRAN FE software [21]. Figure 3 shows the FE model without the polyester skin. The main wing spar (located at 22.5% of the chord) and the rear spar (located at 68.2%) are modeled using plate elements. The ribs are modeled as beam elements. Similarly, the LE beam that connects the rib noses and the short trailing-edge beams (linking the two first ribs to the base of the wing) are modeled with beam elements. The skin supports at the root and the tip of the wing are modeled with plate elements. The loading beam at the tip of the wing is fixed to the outermost rib by rigid connections. The servos (four servos, with each weighing 0.0126 kg), the IMU, and the safety weight on the loading bar (0.01 kg) are modeled as concentrated masses.

The control surfaces are modeled as frames connected with a rib in the center and covered with a plate element on one side (see Fig. 3b). The flap spar connects to the wing's rear spar with rigid elements and with a free DOF of rotation. The flap horn is represented with beam

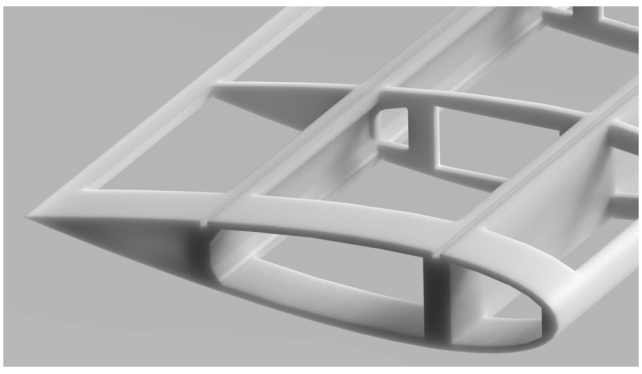

Fig. 2 FOS channels on CAD model.

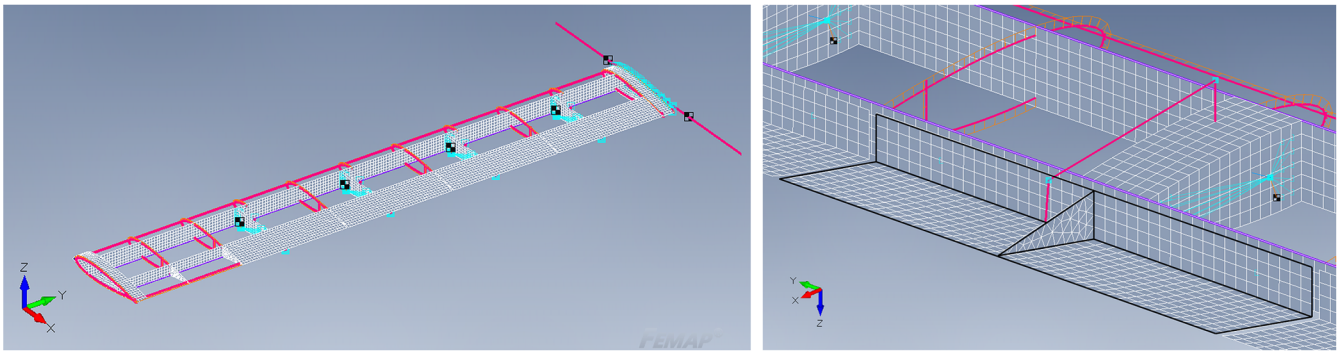

a) b)

Fig. 3 Finite element model of a) wing and b) zoomed-in view of the flap.

Table 1 Material properties

Material	Density, kg/m^3	Young's modulus, MPa	Poisson's ratio	Yield strength, MPa
Nylon-12	900	1800	0.3	46
Polyester	Negligible	2200	0.3	80

elements attached to the symmetry axis of the flap. The servo horn and the flap horn are connected to the push rod via rigid elements with an open DOF to enable rotation between the horn and the push rod. A torsional spring with stiffness of $k_T = 28{,}700\ (\mathrm{N}\cdot\mathrm{m})/\mathrm{rad}$ between the servo horn and the servo represents the static servo stiffness.

The FE model was adapted to static loading and GVTs by modifying the Nylon-12 and polyester material properties as presented in Table 1. The static loading test and GVTs as performed in the wind tunnel are detailed in Appendix A.

B. Aerodynamic Model

The aerodynamic model was realized in ZAERO software using the ZONA6 panel method [22]. The aerodynamic model, shown in Fig. 4, has 16 chordwise and 42 spanwise panels. The wingtip bar is not modeled because it has a negligible contribution to the aerodynamic forces.

C. Free-Vibration Analysis

Free-vibration analysis was carried out in NX NASTRAN. GVTs were performed for the wing with and without the polyester skin to validate the dynamic FE model. In the GVT, the free-vibration responses of several IR reflectors located over the wing's main and rear spars were recorded by the MRS and analyzed for their spectral content. Table 2 shows the structural modes and frequencies, with the skin, in comparison with the GVT results. Additional GVTs were performed in the wind tunnel, as discussed in Appendix B.

Table 2 Structural frequencies for FE model and GVT

Mode	Description	FE model, Hz	GVT, Hz
1	First bending	4.47	4.48
2	First torsion	18.7	18.0
3	First in-plane bending	22.4	22.0
4	Second bending	29.6	29.7

D. Stress Analysis

Stress analysis was performed to ensure that the wing structure can withstand the maximal loads expected during the wind-tunnel test. These occur at the nominal conditions ($\alpha = 5$ deg and $V = 35$ m/s) with the outboard control surface deflected to its maximum positive value ($\delta_4 = 30$ deg). The aerodynamic loads were computed in ZAERO and applied to the structure in a NASTRAN stress analysis. The resulting stresses were compared with the nylon material yield stress of $\sigma_y = 46$ MPa. Figure 5 shows that the maximum von Mises stress in the nylon structure is 30 MPa. This translates to a safety factor for the material of 1.53. At the polyester skin, a maximum von Mises stress of 44.4 MPa was computed at the root of the wing on the tensioned side, translating to a safety factor of 1.17.

E. Flutter Analysis

The wing was tested with two 10 g weights on the wingtip loading bar: one at the LE, fixed to the bar with a bolt; and the other at the trailing-edge side, free to move on the bar. The trailing-edge weight served as a safety mechanism. At flutter onset, as the wing twist oscillations grow, the weight flies off, and flutter stops. Table 3 show the flutter speeds for each weight configuration.

Figure 6 shows an ω–V–g plot, presenting the variation of the aeroelastic frequencies and damping values of the first four aeroelastic modes as a function of airspeed for the tested configuration with both the LE and TE weights. Flutter analysis was performed

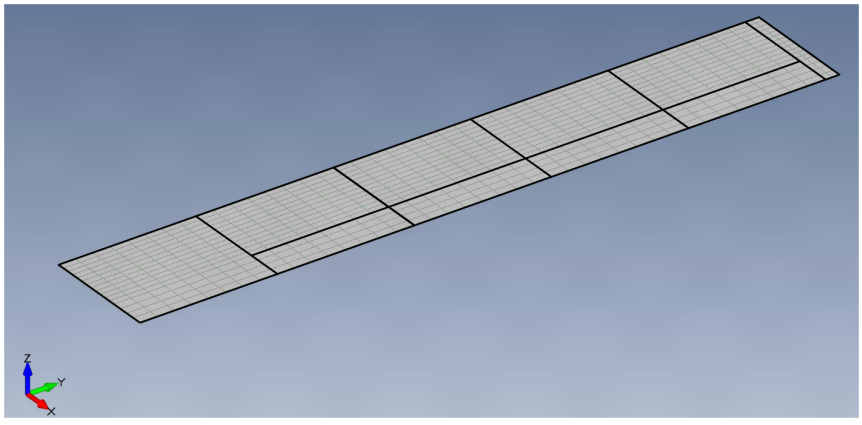

Fig. 4 Aerodynamic panel model realized in ZAERO.

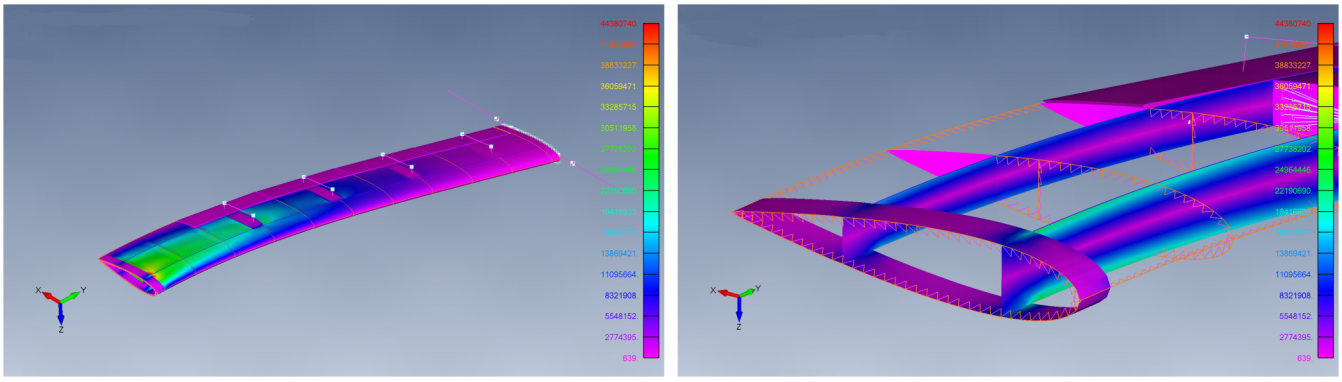

a) b)

Fig. 5 Stresses at the maximum loading conditions: a) polyester skin stress and b) Nylon-12 stress.

Table 3 Flutter characteristics without and with weights

Configuration	Speed, m/s	Frequency, Hz	Flutter mechanism
Clean	40	15.8	First bending–first torsion
LE + TE weights	40	13.6	First bending–first torsion
LE weight	47	14.6	First bending–first torsion

with 10 modes. Only the first four are shown in Fig. 6 for clarity. An abrupt first-bending first-torsion flutter is predicted at 40 m/s, with a frequency of about 13 Hz.

IV. Computational Trim Optimization

The goal of the computational trim optimization is to examine the proposed optimization process by following the experimental procedure using computational data. The computational trim optimization process is as follows: Sensitivities of the lift coefficient and the wing's first-bending modal coordinate ξ_1 to control-surface deflections are computed in ZAERO at the nominal trim conditions. These sensitivities are used in a MATLAB-based optimization that reduces the wing's first-bending modal coordinate ξ_1 below a defined value, while keeping the nominal lift coefficient and while minimizing the control-surface usage, at some nominal conditions.

The optimized control-surface deflections are used in a ZAERO analysis to compute the lift distribution over the wingspan. The aerodynamic load is then used in a NASTRAN analysis to compute the strains at selected locations over the front and rear spars, where the FOSs are located in the experimental setup. The strains are used to compute the modal coordinates using the least-squares process of Eq. (8), with computational strain modes from free-vibration analysis.

In the computational trim optimization, the sensitivities, the strains, and the strain modes are computed. In the experimental case, these are measured or computed from measured quantities. Hence, the experimental trim optimization is independent of a FE model.

A. Baseline Trim Configuration

The nominal conditions were set as $\alpha = 5$ deg, $\delta_i = 0$ (the control surfaces are not deflected), an airspeed of 35 m/s, and a standard sea-level density of 1.225 kg/m^3 (dynamic pressure of 750 Pa). For these conditions, the lift coefficient on the deformed wing is $C_{L_{\text{nom}}} = 0.523$. The modal coordinate of the first wing-bending mode equals $\xi_{1_{\text{nom}}} = 3.23\text{E}-2$, and the corresponding wingtip vertical displacement is 0.1 m. The wingtip twist angle at these conditions is 6.4 deg.

B. Trim Optimization Results

Table 4 presents the lift coefficient due to unit displacement of each of the trim effectors for the rigid and flexible configurations. These derivatives were computed in a ZAERO static aeroelastic analysis of the clamped wing at the nominal conditions. The control surfaces are labeled δ_1–δ_4 from the root outward. A positive deflection is defined downward. A positive deflection of the trailing-edge surfaces leads to a negative (nose down) twist of the wing. Hence, the lift generated by a positive deflection of the control surfaces is positive for the rigid wing and decreases for the elastic wing due to the negative twist of the entire wing section. Surface δ_1, which is closest to the wing root, is the most effective in lift and generates minimal wing deformation per unit deflection. Surface δ_4, which is closest to the tip, is the least

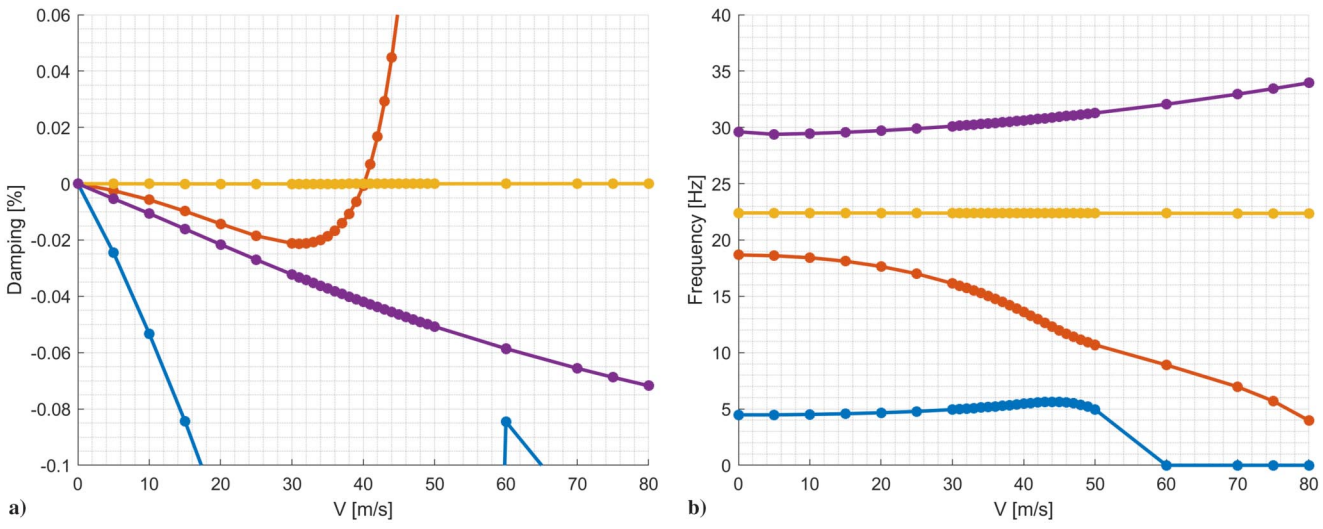

a) b)

Fig. 6 Flutter analysis: ω-V-g plot. Wing with LE and TE weights configuration.

Table 4 Simulated aerodynamic and structural coefficients

Variable	Coefficient	Flexible	Rigid
δ_1	$C_{L_{\delta_1}}$	1.078E−2	1.292E−2
	$\partial\xi_1/\partial\delta_1$	2.690E−4	— —
δ_2	$C_{L_{\delta_2}}$	9.425E−3	1.259E−2
	$\partial\xi_1/\partial\delta_2$	4.928E−4	— —
δ_3	$C_{L_{\delta_3}}$	8.093E−3	1.182E−2
	$\partial\xi_1/\partial\delta_3$	7.732E−4	— —
δ_4	$C_{L_{\delta_4}}$	5.552E−3	9.37E−3
	$\partial\xi_1/\partial\delta_4$	8.621E−4	— —

effective in lift (likely due to downwash) but generates the largest wing deformation. Because the goal is to generate a required amount of lift with constrained wing deformation, the optimal condition will be achieved with larger positive deflections of the inboard surfaces, shifting the lift inboard.

Three optimization cases are computed in which the trim optimization attempts to generate the same amount of lift as in the baseline configuration at the nominal conditions, $C_L = C_{L_{\text{nom}}}$, while reducing the wing deformations to 30, 20, and 10% of the baseline deformation. The constraints are set on the wing first-bending-mode coordinate, requiring $\xi_1 = 0.3\xi_{1_{\text{nom}}}$, $\xi_1 = 0.2\xi_{1_{\text{nom}}}$, and $\xi_1 = 0.1\xi_{1_{\text{nom}}}$ in cases 1–3, respectively. The trim variables' vector includes the four trailing-edge control surfaces $\{\delta\} = \{\delta_1, \delta_2, \delta_3, \delta_4\}^T$. The objective function is minimization of the control effort [Eq. (6)] with a relative cost of $\{d\} = \{1, 1, 1, 1\}^T$ (i.e., equal importance of the variables because we are not prioritizing the use of any control surface). In a free-flying configuration, these costs could be significant. For example, to save the outermost surfaces for turn maneuvers, their cost could be set higher than the others. In the case of the current study of a clamped wing in the wind tunnel, there is no special significance to setting a nonuniform cost.

Each control surface was subject to travel limits of −30 to 30 deg. Hinge moments were not set as constraints in the optimization problem. ZAERO analysis has shown that the control-surface hinge moments at the maximum deflections are about one order of magnitude lower than the maximum allowable values for the servo torque (which is $0.24\,\text{N}\cdot\text{m}$).

Tables 5–7 present the trim optimization results for the three cases. Table 5 shows the computed ξ_1 modal coordinate that, in all cases, is smaller than the constraint value ξ_1^{maxreq}. In all cases, the lift coefficient

Table 5 Simulated optimization: maximal required and computed ξ_1 in the three optimization cases

	Case 1	Case 2	Case 3
$\xi_1^{\text{maxreq.}}$	9.7E − 3	6.4E − 3	3.2E − 3
$\xi_1^{\text{opt.}}$	9.4E − 3	6.1E − 3	2.9E − 3

Table 6 Simulated optimization: control-surface deflections (in degrees) in three optimization cases (not to scale)

Control surface, deg	Case 1	Case 2	Case 3
δ_1	18.9	21.7	24.4
δ_2	4.5	5.1	5.8
δ_3	−16.7	−19.1	−21.5
δ_4	−20.0	−22.9	−25.7

Table 7 Simulated optimization: modal coordinate values in the three optimization cases

	Case 1	Case 2	Case 3	Baseline
ξ_1: first bending	9.386E − 3	6.117E − 3	2.854E − 3	3.225E − 2
ξ_2: first torsion	1.307E − 3	1.313E − 3	1.319E − 3	1.265E − 3
ξ_3: fore/aft first bending	8.445E − 5	8.349E − 5	8.255E − 5	9.108E − 5
ξ_4: second bending	1.264E − 3	1.299E − 3	1.335E − 3	1.013E − 3

is the required value of $C_L = C_{L_{\text{nom}}} = 0.523$. Table 6 presents the optimized control-surface deflections. These deflections are considerable, even for case 1. Although these control-surface setups achieve the required wing deformation reduction, they are likely to increase the drag significantly. Such a setup could be used to decrease the wing deformations momentarily but would be inefficient in a steady trimmed flight.

Table 7 presents all the modal coordinates at the three optimized states. We note that as a more stringent constraint is imposed on the ξ_1 coordinate, while keeping a fixed lift coefficient, the optimal shape has relatively more second-bending participation. The different optimal wing shapes are presented in Fig. 7.

V. Wind-Tunnel Experiment

The wind-tunnel experiment had two phases. In phase one, the control-surface lift effectiveness was estimated at different airspeeds. This was intended to assure that the control surfaces were performing as expected, provide an estimate of the real control-surface lift sensitivities compared with the computational ones, and provide an estimate of the control-surface loss of effectiveness with increasing dynamic pressure.

The second phase of the experiment included the trim optimization with steps as follows: The wind-tunnel was operated at the nominal conditions ($\alpha = 5$ deg, $\delta_i = 0$, and $V = 35$ m/s) to determine the experimental baseline lift-coefficient value and wing deformation. The latter was determined from the strain data and compared with the deformation as captured by the MRS. Sensitivities of the lift coefficient and the wing's first-bending modal coordinate ξ_1 to control-surface deflections were estimated by deflecting each control surface through its negative and positive ranges at the nominal conditions. These sensitivities were used in the MATLAB-based trim optimization, in which a constraint was set to reduce the wing's first-bending modal coordinate to 0.7 of its nominal value while keeping the nominal lift coefficient and minimizing the control-surface usage. In the experiment, the constraint on ξ_1 was less stringent than in the computational study (where ξ_1 was limited to 0.3, 0.2, and 0.1 of $\xi_{1_{\text{nom}}}$) because the actual control surface effectiveness was significantly lower than the computed value. The trim optimization provided the required control-surface deflections. The wind tunnel was operated again at the nominal conditions, the control surfaces were deflected to their computed optimal deflection, the lift was measured via the force balance, and the wing's bending modal coordinate was determined from the strain data and compared to that from the MRS.

Figure 8a shows the tested wing model, and Fig. 8b shows an earlier model of the wing mounted on the balance adapter in the wind tunnel. The following subsections describe the instrumentation and tests.

A. Instrumentation

Figure 9a shows the instrumented wing, with the mounted servos, without the flaps and polyester skin. Two strain-measuring optical fibers are embedded in cavities on one side of the front and rear spars (seen in the zoomed-in photograph in Fig. 9b). The sensors are discrete FBG measuring strains at 15 locations on each spar. The first sensor is placed 20 mm outboard of the root (on both the front and rear spars), and the distance between consecutive sensors is 35 mm. The details of the layout of the fibers are similar to those described in Ref. [14]. Figure 10 shows the glowing FOSs (under red

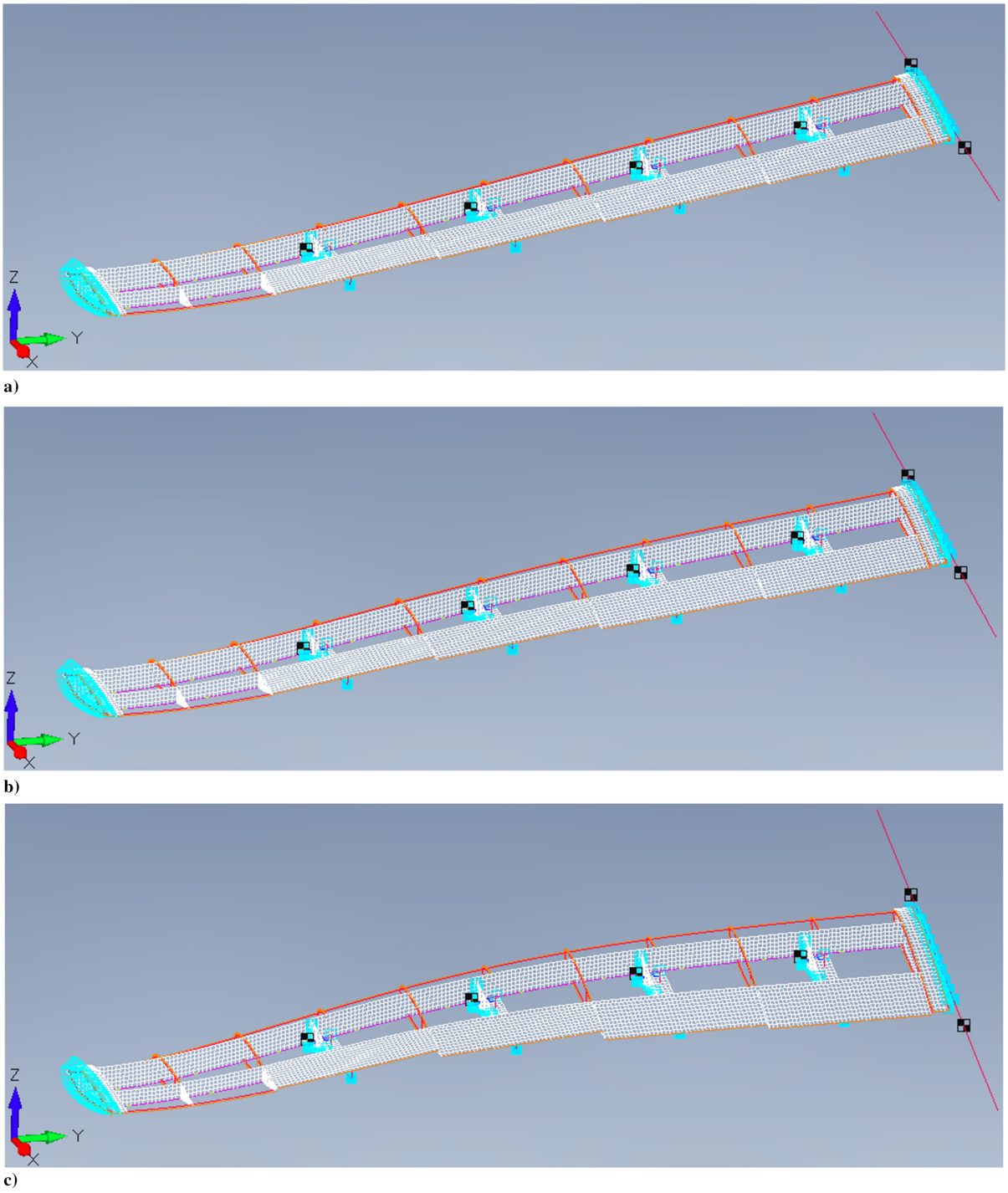

Fig. 7 Optimal wing shape for a) case 1, b) case 2, and c) case 3.

in-fiber illumination) on the front and rear spars, indicating their locations.

In Fig. 8, the gray markers are the IR reflectors used by the MRS to capture the wing's deformed shape. The wing was also instrumented with an IMU (seen in Fig. 9b) for measuring accelerations and rates close to the wingtip. Integral forces and moments were measured by a five-component sting force balance attached perpendicular to the wind-tunnel floor. The wing was connected to the balance via an adapter, as shown in Fig. 8b.

B. Control-Surface Effectiveness

The control-surface effectiveness was estimated experimentally at different airspeeds. After ramping the airspeed, each control surface was deflected to negative -30 deg, then to $+30$ deg in increments of $+10$ deg, and back to zero. This was done sequentially to surfaces 1 to 4. Figures 11–14 show the incremental lift coefficient versus control-surface deflection, and versus time, for each tested airspeed. The lift at zero control-surface deflection was deducted from the measurements such that the plots only reflect the control surface's lift. We note that the incremental lift coefficient did not return to zero when the control-surface deflection was returned to zero.

At 10 m/s, C_L is mostly linear with control-surface deflection. At the higher speeds, the response is nonlinear such that a larger deflection results in a larger-than-linear lift. This is more significant for the inboard surfaces than for the outer. Flap 4 (closest to the wingtip) is the least effective flap, likely due to the downwash effect. For the trim optimization, the sensitivities were assumed linear and the average value was used.

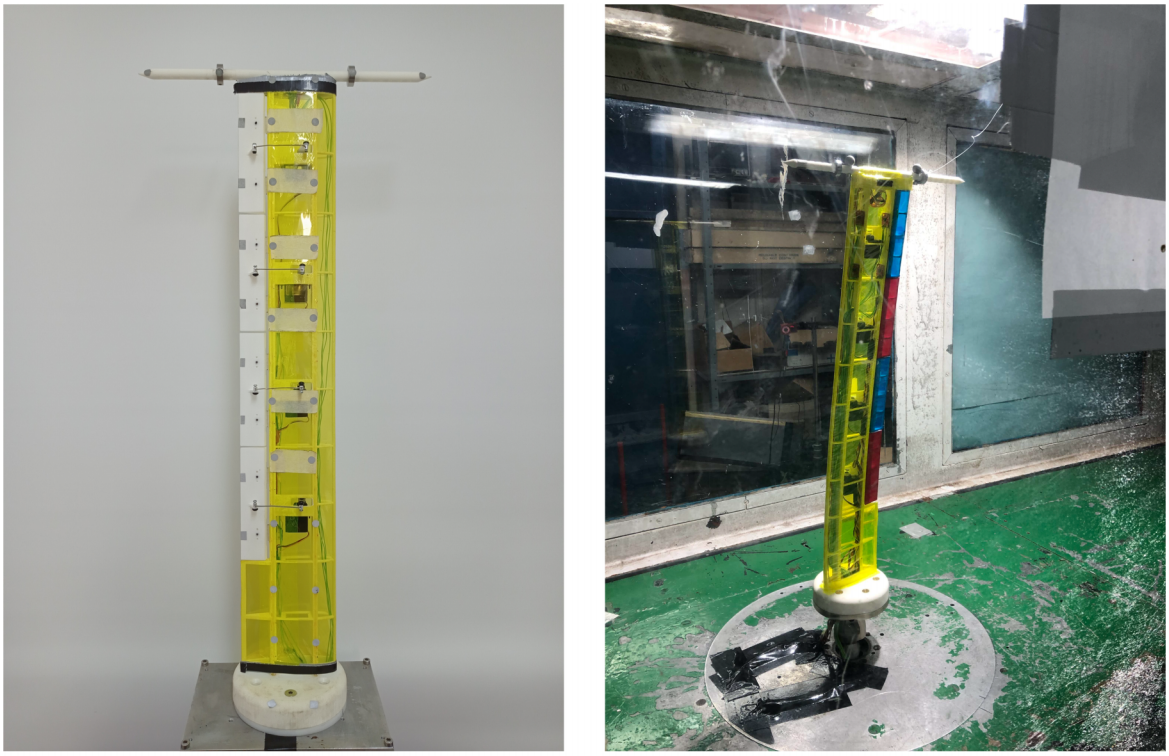

a) b)

Fig. 8 Photographs of a) wing model and b) wing in the wind tunnel.

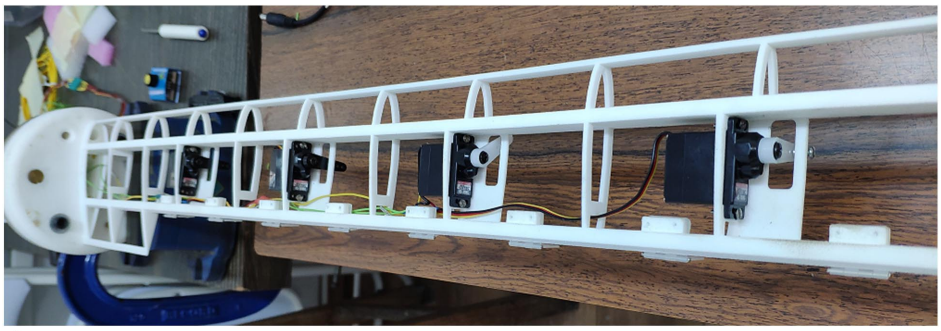

a)

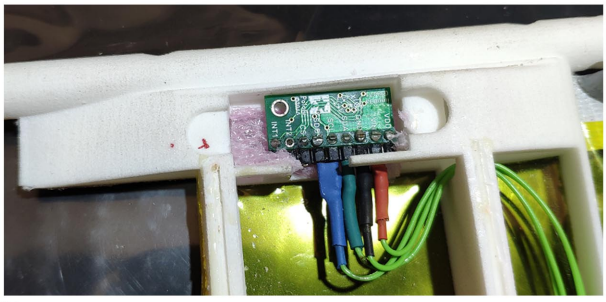

b)

Fig. 9 Photographs of a) instrumented bare wing and b) zoomed-in view of the wingtip.

Figure 15 shows the computational and experimental control-surface effectiveness with airspeed. The trend of reduced effectiveness with airspeed is similar. However, the computational values are about three times larger than the experimental ones. This could be attributed to the low Reynolds number of the test and to the gap between the control surfaces and the main wing. It is also possible that the control-surface actual deflections were not as commanded. The experimental trim optimization was based on the experimental control-surface sensitivities (both the lift-coefficient sensitivity and the first-bending modal coordinate sensitivity) that are presented in the next subsection.

C. Experimental Trim Optimization

The experimental trim optimization process was as follows: The wind-tunnel was operated at the nominal flow conditions to determine the baseline lift coefficient and wing deformation. At these conditions, the lift coefficient and the wing's first-bending sensitivities to control-surface deflections were estimated by deflecting each

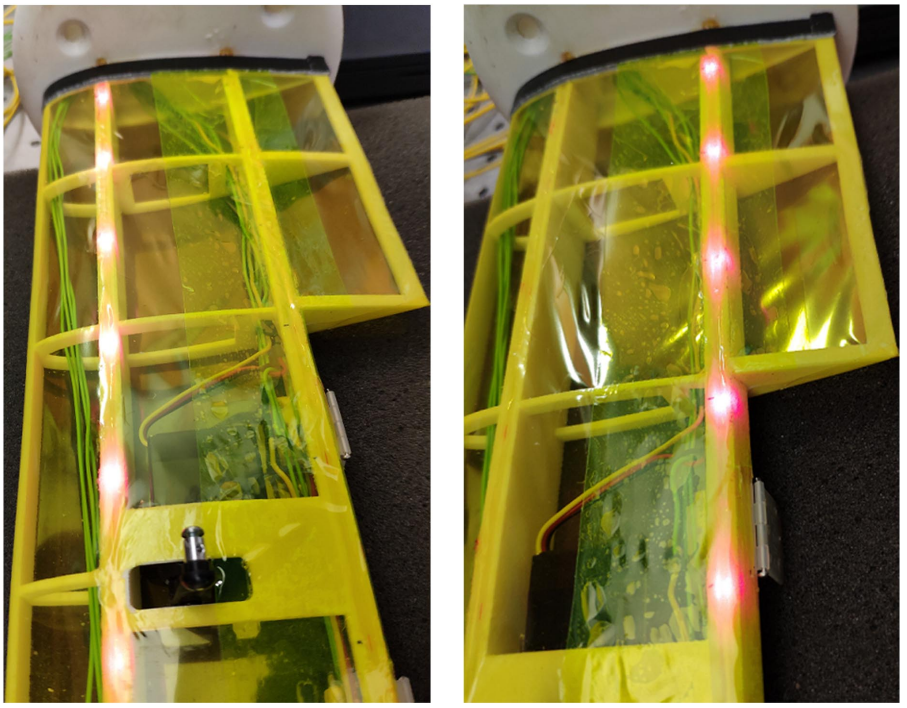

a) b)

Fig. 10 Glowing FOSs showing the sensor locations on the front and rear spars.

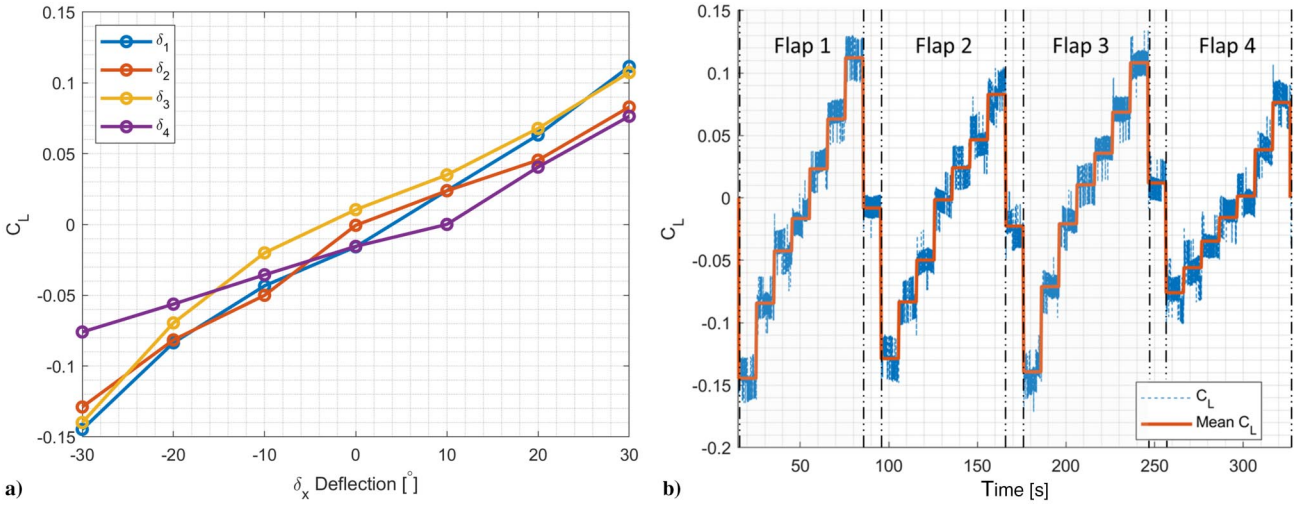

a) b)

Fig. 11 C_L vs a) flap deflection and b) time; $V = 10$ m/s.

control surface in steps, covering the range between -30 to $+30$ deg. These sensitivities were used in a MATLAB-based optimization that determined the control-surface deflections required to reduce the wing's first-bending modal coordinate ξ_1 to 70% of the baseline value at the nominal conditions, or lower, while keeping the nominal lift coefficient and while minimizing the control-surface usage. The wind tunnel was operated again at the same nominal conditions. The optimal control-surface deflections were commanded, and the lift and strains were recorded. The latter were converted to modal coordinates. The results were studied to evaluate how successful the trim optimization was, and strain data were used to estimate the deformations.

The nominal conditions were set as $\alpha = 5$ deg, $\delta_i = 0$ (no control-surface deflection), and an airspeed of 25 m/s. The corresponding dynamic pressure, as measured at the wind tunnel, was 387 Pa. For these conditions, the lift coefficient on the deformed wing, as indicated by the balance system, was $CL_{\text{nom}} = 0.42$. Based on the recorded strain data, the first wing-bending mode's modal coordinate was $\xi_1 = -1.68\text{E}{-2}$ and the corresponding wingtip vertical deformation was 4.7 cm. The estimation of ξ_1 was based on the strain data that were mapped to modal coordinates using Eq. (8) with the experimental strain modes (those of the wing on the balance adapter; see Fig. B4). The wing deformation was validated by the MRS.

In the test, the wing deflections were significantly larger than in the analysis. The exact source of discrepancy between the computational and test models could not be pinpointed. Therefore, the nominal conditions in the test were set at a lower dynamic pressure than in the computational study to avoid overstressing the wing structure.

Figure 16a shows the lift sensitivity to control-surface deflection at the nominal conditions, and Fig. 16b shows the lift coefficient versus time as the four surfaces were deflected. Figure 16 shows that the lift coefficient does not change linearly with control-surface deflection

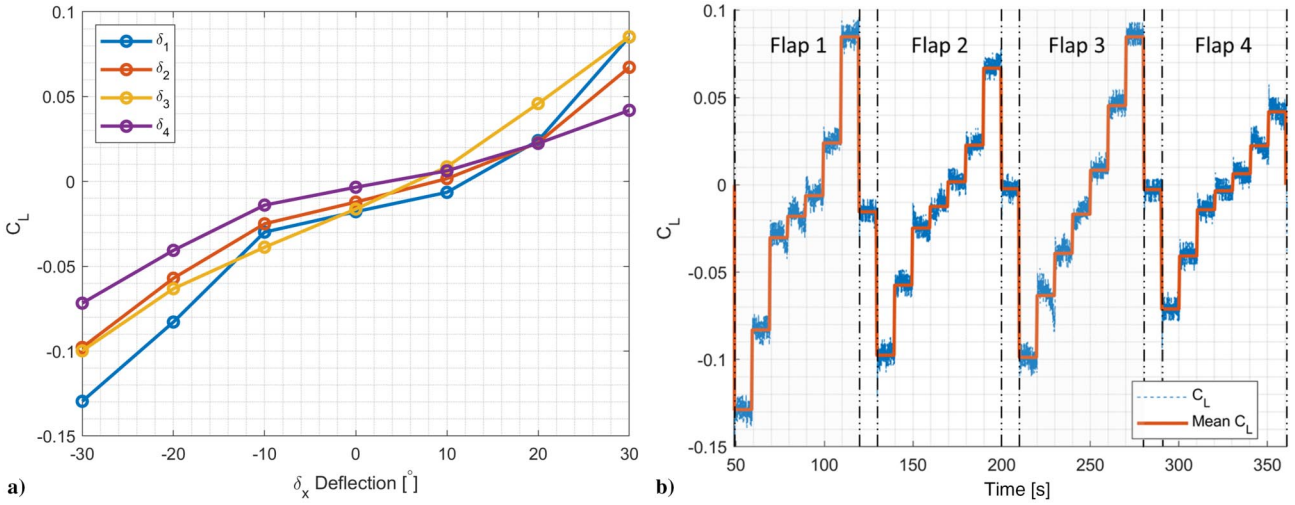

Fig. 12 C_L vs a) flap deflection and b) time; $V = 20$ m/s.

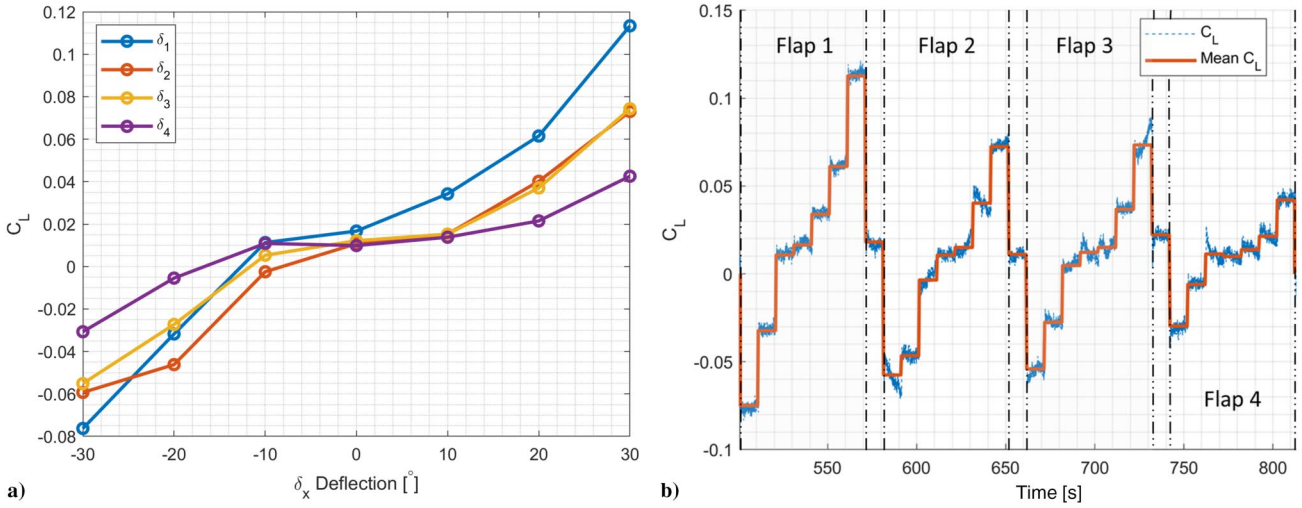

Fig. 13 C_L vs a) flap deflection and b) time; $V = 30$ m/s.

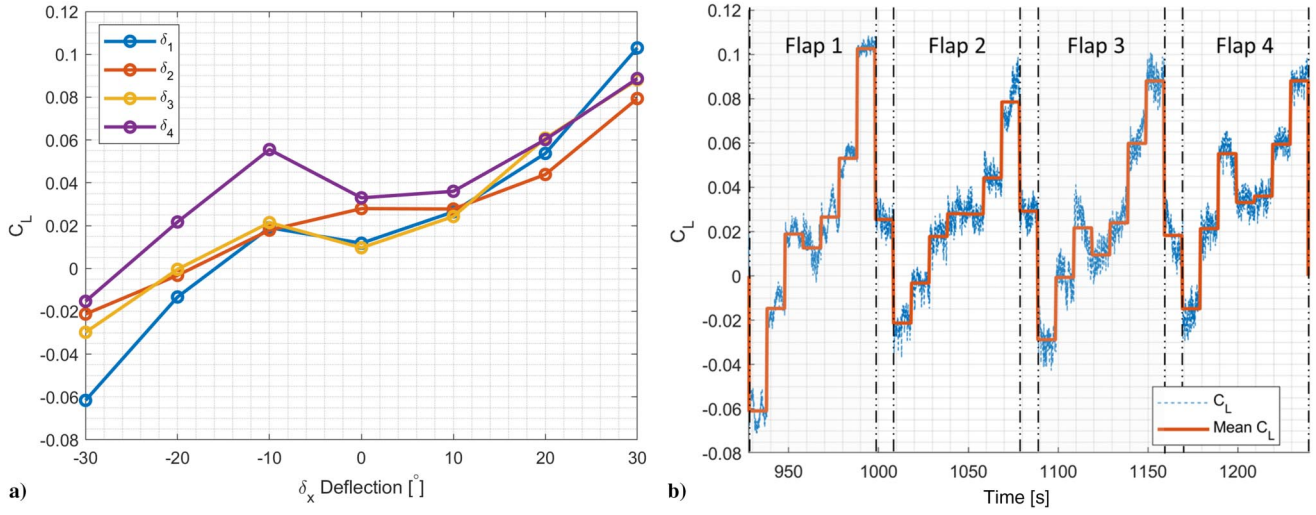

Fig. 14 C_L vs a) flap deflection and b) time; $V = 35$ m/s.

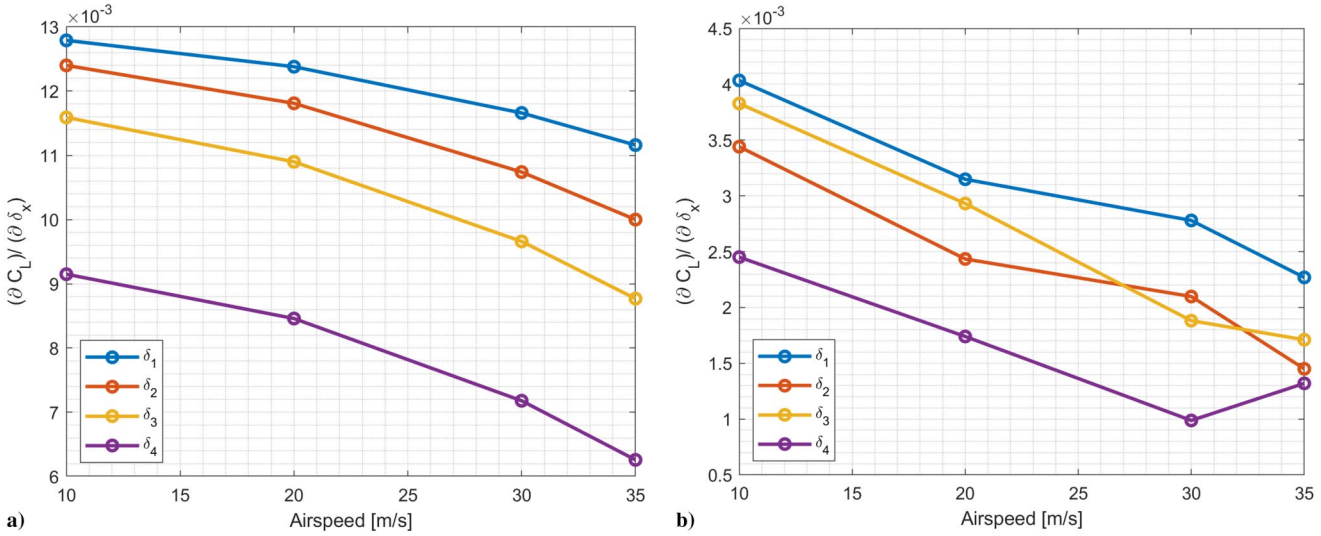

Fig. 15 Control-surface effectiveness versus airspeed: a) Computational, and b) experimental.

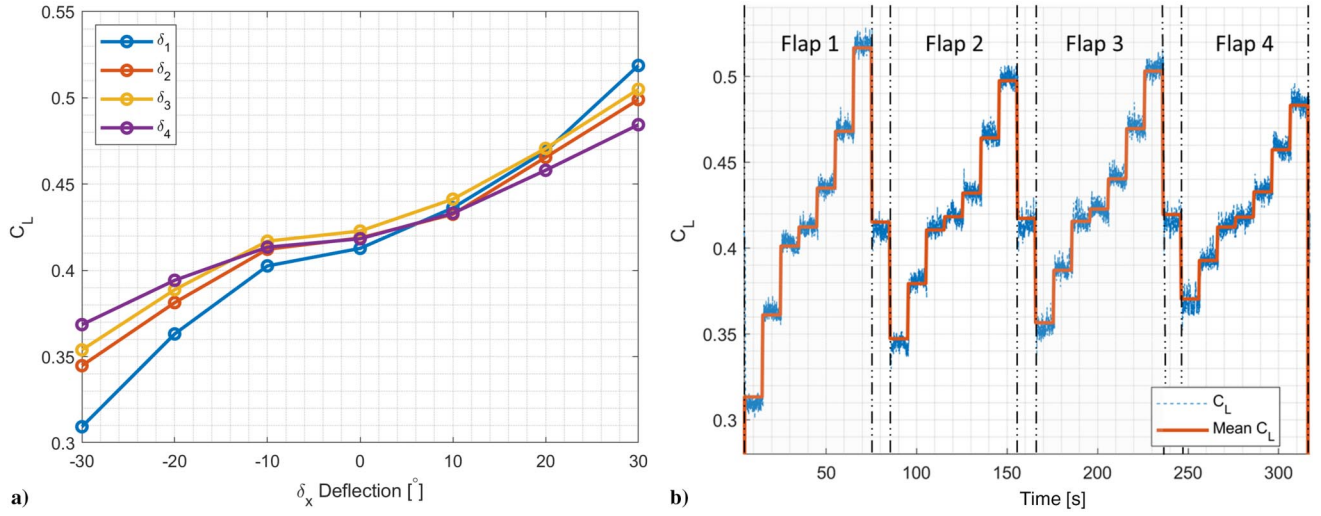

Fig. 16 Representations of a) C_L vs flap deflection and b) flap deflections vs time; nominal conditions (5 deg AOA, and 25 m/s).

and the lift does not return to the nominal value when a control-surface deflection is returned to zero. The lift due to control-surface deflection in Fig. 16a was used to extract linearized sensitivities for the optimization. The linear derivatives were computed in two ways: once by averaging the lift line slopes from all the deflection angles; and once by averaging the lift at zero control-surface deflection for all the surfaces, and then averaging the lift line slopes from all the deflection angles with respect to that averaged zero deflection lift value. In what follows, we refer to the first as noncorrected flap coefficients and to the latter as corrected flap coefficients. The corrected and noncorrected derivatives are presented in Table 8. Similarly, Fig. 17a shows the first wing-bending-mode displacement sensitivities to control-surface deflection at the nominal conditions, which were computed from the measured strains using Eq. (8) and the experimental strain modes (Fig. B4).

Figures 18–20 show results from three trim optimization cases. The first two were based on the corrected control-surface coefficients, and the third was based on the uncorrected ones. The figures show the lift coefficient (blue) on the left axis and the wingtip deflection of the main spar on the right axis (orange) over time. The measured data are presented in thin dashed lines and the averaged data in thick lines. An optimization attempt started with setting the wing to a 5 deg AOA. Then, the airspeed in the wind tunnel was ramped to a nominal 25 m/s. Once the flow settled, the optimal control-surface deflection was commanded. After a few more seconds, the control-surface deflection was set back to zero. Figures 18–20 show the entire optimization run-through. The optimization results are summarized in Table 9.

For the first two optimization attempts (which were based on the corrected flap coefficients), the following flap deflections were computed $\delta_1 = 30.0$ deg, $\delta_2 = 12.9$ deg, $\delta_3 = -30.0$ deg, and $\delta_4 = -30.0$ deg. The first optimization process is presented in Fig. 18. The optimization brought the wingtip from an initial

Table 8 Corrected and noncorrected control-surface derivatives; nominal conditions (5 deg AOA, and 25 m/s)

	Corrected	Noncorrected
C_{L_α}	8.36E−2	8.45E−2
$C_{L_{\delta 1}}$	2.6E−3	3.1E−3
$C_{L_{\delta 2}}$	1.9E−3	2.3E−3
$C_{L_{\delta 3}}$	1.9E−3	2.3E−3
$C_{L_{\delta 4}}$	1.5E−3	1.8E−3
ξ_{1_α}	−6.08E−3	−6.17E−3
$\xi_{1_{\delta 1}}$	−7.38E−5	−8.54E−5
$\xi_{1_{\delta 2}}$	−1.23E−4	−1.46E−5
$\xi_{1_{\delta 3}}$	−1.92E−4	−2.18E−5
$\xi_{1_{\delta 4}}$	−2.27E−4	−2.55E−5

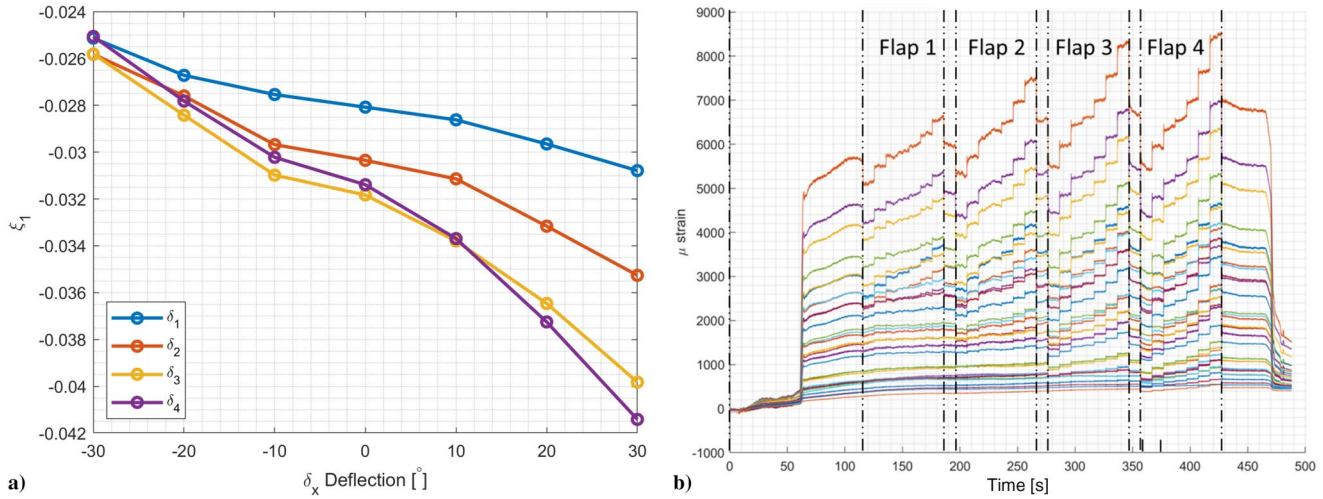

Fig. 17 Representations of a) ξ_1 vs flap deflection and b) μ-strain vs time; nominal conditions (5 deg AOA, and 25 m/s).

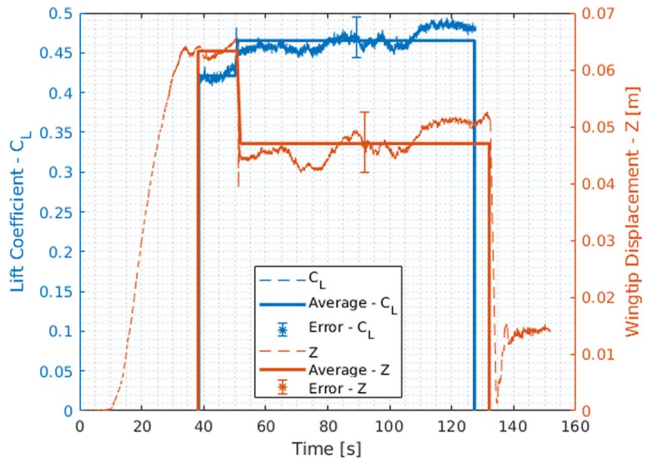

Fig. 18 Optimization results for case 1, based on corrected control-surface coefficients.

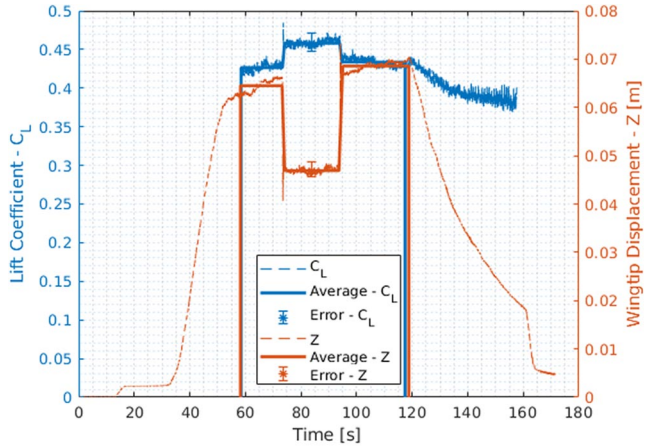

Fig. 19 Optimization results for case 2, based on corrected control-surface coefficients.

6.3 cm deflection down to an average displacement of 4.7 cm$\pm$ 0.5 cm. The lift coefficient was increased from $C_L = 0.42$ to $C_L = 0.47 \pm 0.025$. Although the deformation was reduced, the goal values were not achieved, and the lift was slightly increased. This is attributed to the low control-surface effectiveness that drove control surfaces 1, 3, and 4 to their maximum allowable deflection, as well as to inaccurate control-surface sensitivities. An additional optimization run (optimization 2) based on the same control-surface

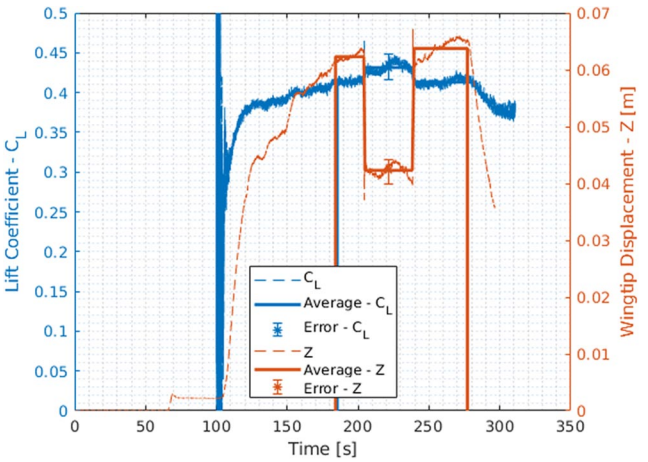

Fig. 20 Optimization results for case 3, based on noncorrected control-surface coefficients.

derivatives is shown in Fig. 19. The results are very close to those of optimization 1. The wingtip deformation was reduced from 6.7 cm down to an average displacement of 4.6 cm + 0.2, −0.1 cm, almost achieving the optimization goal. The lift coefficient was increased from $C_L = 0.42$ to $C_L = 0.46 + 0.02, -0.01$.

Optimization 3 was based on the noncorrected flap coefficients. The following optimal flap deflections were computed: $\delta_1 = 30.0$ deg, $\delta_2 = 12.0$ deg, $\delta_3 = -30.0$ deg, and $\delta_4 = -30.0$ deg. Figure 20 shows the optimization process. The optimization brought the wingtip from initially 6.3 cm down to 4.2 cm $\pm$ 0.2 cm, achieving the

Table 9 Trim optimization results; nominal conditions (5 deg AOA, and 25 m/s)

	Optimization 1	Optimization 2	Optimization 3
$\xi_{\text{nom.}}$	−2.41E − 2	−2.41E − 2	−2.27E − 2
ξ_{target}	−1.69E − 2	−1.69E − 2	−1.59E − 2
ξ_{trim}	−1.77E − 2	−1.74E − 2	−1.49E − 2
ξ deviation, %	4.7	2.9	— —
$C_{L_{\text{nom.}}}$	0.42	0.43	0.41
$C_{L_{\text{trim}}}$	0.46	0.46	0.43
C_L deviation, %	10.5	6.5	4.3
Displacement nominal, m	0.063	0.067	0.063
Displacement target, m	0.045	0.045	0.045
Displacement trim, m	0.047	0.046	0.042
Displacement deviation, %	4.5	4.3	— —

optimization deformation constraint. The lift coefficient was slightly increased from $C_L = 0.42$ to $C_L = 0.43 \pm 0.02$. Considering the minor deviation in the lift coefficient, the optimization goal was reached.

We note the discrepancies between the computational and experimental models. These could be attributed to the wing's initial deformed shape (imperfections resulting from the additive manufacturing process), gaps between the control surfaces and the main wing, and the low Reynolds numbers in which the wing was tested. It is also possible that the control-surface deflections were not as commanded. As a result, the computational optimization gains could not be fully realized in the experiment. However, the experimental optimization did present a 30% reduction in the deformed bending shape of the wing while producing the required nominal lift and demonstrating the feasibility of trim optimization based on FOS strain data. The control-surface deflections required to reduce the wing deformation were very large, which would likely significantly increase the wing's drag. As noted in the computational part of the study, such a setup could be used to reduce the wing deformations momentarily but would be inefficient in a steady trimmed flight. It primarily indicates that large control surfaces are not the optimal means for controlling the aerodynamic load distribution over the wingspan, and shape optimization could possibly be better achieved with strain actuators or by distributed multiple control surfaces [23].

D. Modal Representation Sensitivity to Strain Modes

One of the significant and most valuable features of the proposed process is that extracting the wing deformations is based solely on experimental data. The study demonstrates how wing deformations are determined from data that include the measured strains and a set of strain modes, where the latter are also extracted experimentally in a GVT (see Appendix B for details on the wind-tunnel GVT). However, the experimentally extracted strain-mode shapes are subject to irregularities and errors resulting from the measurement and processing limitations. This section examines the computed wing deformation's sensitivity to variations in the strain-mode set used to calculate it. We do this by comparing the calculated modal coordinate values based on three different strain-mode sets. The comparison is done at the nominal conditions of $\alpha = 5$ deg, $\delta_i = 0$ (no control-surface deflection), and an airspeed of 25 m/s. Figures 21a–21c show the three mode sets, where all modes are similarly normalized to a maximum unit strain. The three mode sets are as follows:

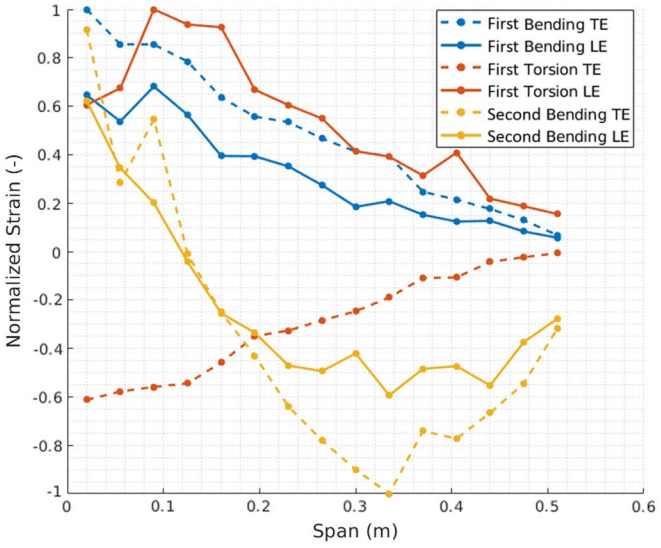

a) Strain modes: experiment with balance

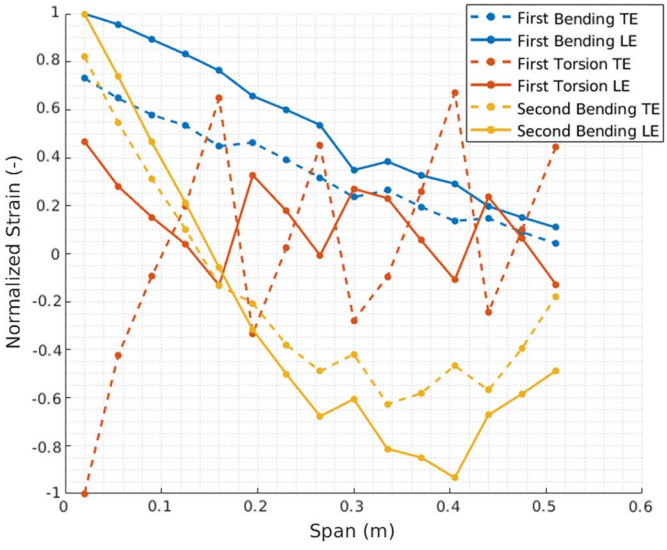

b) Strain modes: computational

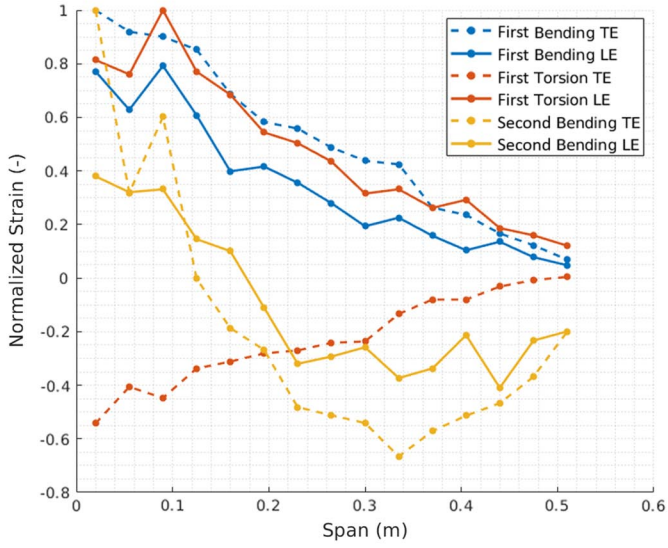

c) Strain modes: experiment without balance

Fig. 21 Three sets of strain modes (experimental and computational) used in strain-to-displacement transformation.

Table 10 Modal coordinate comparison using different sets of strain modes

	Experiment with balance	Computational	Experiment without balance
First bending $\xi_{1_{norm}}$	0.00374	0.00366	0.00324
First torsion $\xi_{2_{norm}}$	0.00157	0.00045	0.00175
Second bending $\xi_{4_{norm}}$	0.00071	0.00074	0.00070

1) The experimental mode set extracted for the wing on the force-balance. This is the mode set that was used for the trim optimization (Fig. 21a).

2) The computational mode set from the FE model (Fig. 21b).

3) The experimental mode set extracted for the wing connected directly to the wind tunnel floor (Fig. 21c).

Each set contains three modes, shown in different colors in Fig. 21. Each mode displays the strains over the front spar in a full line (labeled LE) and the strains over the rear spar in a dashed line (labeled TE). Each strain mode is normalized by the largest absolute strain value.

Table 10 shows the modal coordinate values for representing a positive deflected pitch-up wing shape. The first bending has the highest participation, regardless of the mode set used. The modal coordinate values are similar for all the mode sets used, other than the torsion coordinate for the computational mode set, which is very low. This happens because of a difference in the pitch deformation between the computational and experimental sets. In the experimental mode sets, the first-bending mode has a pitch-down deformation, indicated by the higher strains in the aft spar (TE), whereas in the computational mode set, the first-bending mode has a pitch-up deformation. The reconstructed shape must have a pitch-up profile. Therefore, when using the experimental mode sets, a higher amount of first torsion is involved.

Figure 22 shows the strains over the wing front and the rear spar (labeled LE and TE, respectively), as measured directly and as reconstructed from the summation of strain modes, using the experimental mode set of the wing on the force balance. Other than close to the wing root area, the match between the measured and reconstructed strains is excellent. Figure 22 shows an additional reconstructed strain plot in which only the first-bending and first-torsion strain modes were used. This results in a significantly less good match, indicating that the second-bending strain mode is significant for the strain distribution. This exercise in modal representation using different mode sets indicates that strain-mode sets that are similar but not exact can be used, provided that a sufficient number of modes is included to represent the deformed shape accurately.

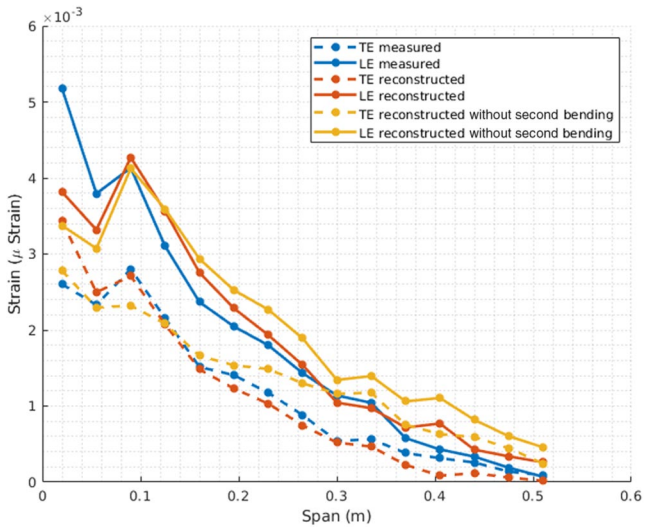

Fig. 22 Reconstructed strains using the experimental modes (on balance).

VI. Conclusions

The paper presented an experimental trim optimization study solely based on measured strain data (via fiber-optic sensing), without resorting to a computational model. A flexible-wing shape was optimized at some flow conditions using four trailing-edge control surfaces. Trim requirements included a constraint on the lift value (as needed for trimmed flight) and a constraint on wing deformation, reducing it significantly compared to the baseline deformation at these flow conditions. The optimization goal was set as minimal total control-surface deflection. The data for the optimization included strain values measured over the front and rear wing spars by closely spaced (35 mm) discrete fiber-optic sensors (FBGs) that were translated to modal wing deformations.

For the study, a rectangular wing with four trailing-edge control surfaces was designed, analyzed, constructed by additive manufacturing, instrumented with fiber-optic sensors, and tested in the wind tunnel. The wing's deformed shape (in modal coordinates) and its sensitivity to control-surface deflections were extracted experimentally based on the measured strains. Together with lift sensitivity to control-surface deflections, measured by a force balance, these were used to compute the overall minimum control-surface deflections (in absolute values) that provide a nominal lift value while constraining the wing's first-bending deformation.

The trim optimization study was performed both computationally and experimentally, where the computational process was designed to replicate the experimental procedure in preparation for the wind-tunnel test. In the computational study, wing deformations at a 5 deg angle of attack and a 35 m/s airspeed were reduced to 30, 20, and 10% of the baseline deformation. In the experimental study, wing deformations at a 5 deg angle of attack and a 25 m/s airspeed were reduced to 70% of the baseline deformation. Due to discrepancies between the computational and experimental models, the computational optimization gains could not be fully realized in the experiment. However, the experimental optimization did present a reduction in the deformed bending shape of the wing while producing the required nominal lift. In both the computational and experimental parts of the study, considerable control-surface deformations were commanded. This primarily indicates that large control surfaces are not efficient for controlling the aerodynamic load distribution over the wingspan. Other means, such as distributed multiple control surfaces, could be used based on a similar technique using strain data.

The strain-to-displacement transformation relies on a set of strain modes. The study showed the effect of using different sets of strain modes from FE analysis and strain-based ground-vibration tests. All yield similar results, where the physical displacement is well represented, provided that a sufficient number of modes is used. When the GVT strain modes are used, the trim optimization has the advantage of only using experimental data.

As a direct continuation of this research study, the trim optimization algorithm could be implemented in a closed-loop control sequence such that the wing shape can be monitored online, based on a flow of strain-data readings from the fiber-optic sensors. Additional performance goals can be realized as well (for example, a structural goal of minimization of root-bending moments). Shape and performance control may be implemented on unmanned aerial systems, contributing both to their safe operation and optimal performance.

Appendix A: Static Loading Test and GVT for Model Calibration

The static loading test involves bending and torsional loading cases. The wing was loaded with weights at the wingtip, at two locations on the wingtip beam, with 1.5 cm ahead of the leading edge and behind the trailing edge. The load was increased in steps up

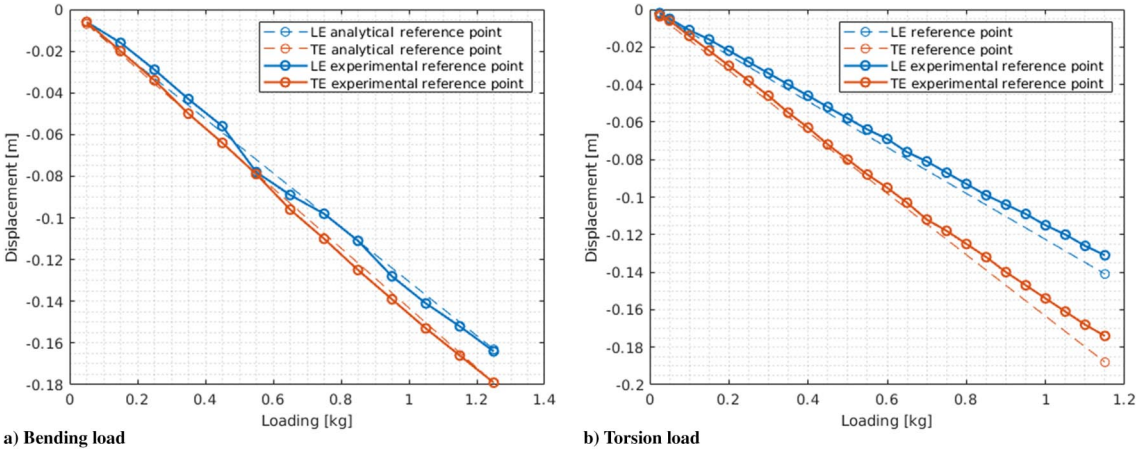

a) Bending load b) Torsion load

Fig. A1 Static loading results for a) bending and b) torsion loading cases.

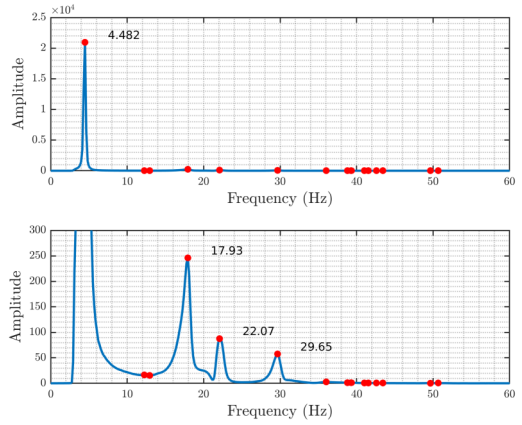

Fig. B1 Frequencies of wing, mounted directly on the wind-tunnel floor, computed by SPOD of strain data. Upper plot shows whole spectrum, and lower plot zooms in on second to fourth frequencies.

to an approximately 15 cm wingtip displacement. For the bending configuration, equal weights were hung on both loading points. For the torsional case, the weights were only applied at the trailing-edge loading point. The deformation was measured at the points where the load was applied via the MRS. The analytical results are compared with the experimental data for the bending and the torsion cases in Fig. A1. The good match between the model and test indicates that for the range of loads examined in the experiment, the structure is linear and the model adequately captures its stiffness. A GVT of the clamped wing was also used for model calibration, as reported in Sec. III.C and in Table 2.

Appendix B: GVT in the Wind Tunnel Using Strain Data

Two sets of GVTs were performed in the wind tunnel. A GVT of the wing clamped directly to the wind-tunnel floor was used to ensure that the setup does not change the wing's dynamics. Another GVT, with the wing attached to the sting balance via an adapter (see Fig. 8), was used to extract the mode shapes of the wing as tested in the wind tunnel. The latter were used in the study to map the measured strains to wing displacements in modal coordinates.

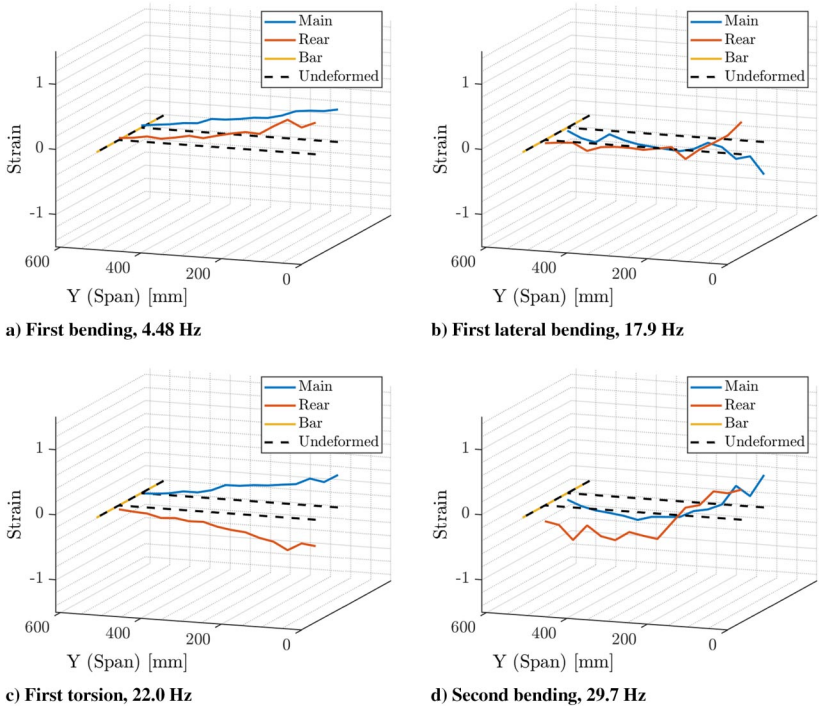

a) First bending, 4.48 Hz b) First lateral bending, 17.9 Hz

c) First torsion, 22.0 Hz d) Second bending, 29.7 Hz

Fig. B2 First four strain modes computed from free-vibration strain data: wing connected directly to tunnel floor.

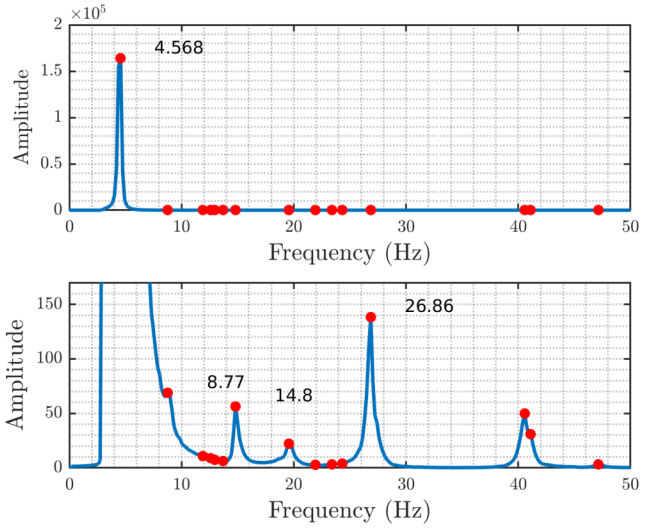

Fig. B3 Frequencies of wing, mounted on force balance, computed by SPOD of strain data. Upper plot shows whole spectrum, and lower plot zooms in on second to fourth frequencies.

The GVTs were based on FOS strain data because these were readily and cleanly available (as compared with the MRS data that were somewhat affected by the wind-tunnel windows and reflections from the transparent skin). Free-vibration time histories of the 30 FBG sensors were recorded in response to initial conditions and analyzed by spectral proper orthogonal decomposition (SPOD) [24] to provide the natural frequencies and strain modes. These are shown in Figs. B1 and B2 for the clamped wing and the wing on the sting balance, respectively. The frequencies match those from the FE model and those measured in a GVT (outside the wind tunnel) using the optical MRS data (Table 2).

The results of the GVT of the wing on the balance (in Figs. B3 and B4, as well as in Table B1) indicate that the sting balance introduced its own dynamics, changing the system's frequencies and mode shapes. We recall it is a sting balance, attached perpendicular to the floor, with the wing attached to it via a metal adapter (Fig. 8b). The sting balance has its natural frequency at about 20 Hz. With the balance adapter and wing on top of it, it is likely that the measured 8.8 Hz frequency in Table B1 is the sting balance mode. The wing's first-bending frequency increased by 2% (possibly a measurement and/or data processing error), whereas the first-torsion frequency decreased significantly by over 30%. Two frequencies of 8.8 and 40.0 Hz are identified that likely belong to the balance adapter dynamics. Although the experiment is static, the modified dynamics affect the data processing because the strain modes are used in converting strains to modal coordinates [Eq. (8)]. In the experimental trim optimization, strain to modal coordinate transformation was based on the modes of the wing on the balance (as tested).

Table B1 Frequencies of wing connected directly to the wind-tunnel floor (without balance adapter) and of wing connected to balance adapter

Mode	Description	Frequency without balance adapter, Hz	Frequency on balance adapter, Hz
1	First bending	4.48	4.57
2	— —	— —	8.8
3	First lateral bending	17.9	— —
4	First torsion	22.0	14.8
5	Second bending	29.7	26.9
6	— —	— —	40.0

Acknowledgments

The study was performed within the Alliance for System Safety of Unmanned Aerial Systems Through Research Excellence Program. The authors would like to gratefully acknowledge the support of the Israeli Civil Aviation Authority in this research project.

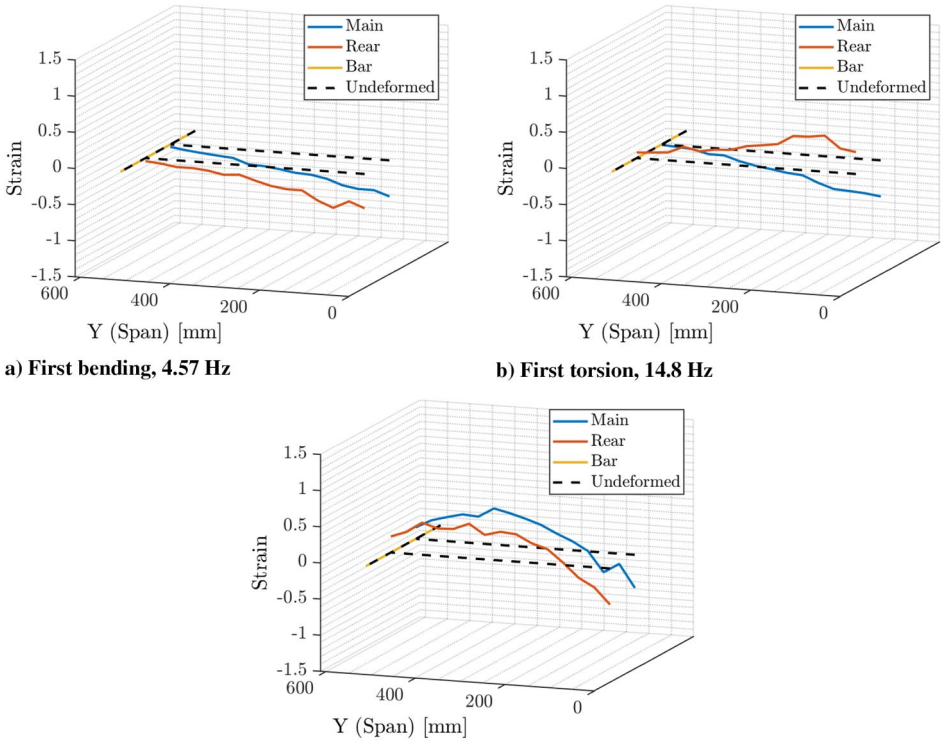

a) First bending, 4.57 Hz

b) First torsion, 14.8 Hz

c) Second bending, 26.9 Hz

Fig. B4 First three strain modes computed from free-vibration strain data: wing connected to balance adapter.

References

[1] Pendleton, E. W., Bessette, D., Field, P. B., Miller, G. D., and Griffin, K. E., "Active Aeroelastic Wing Flight Research Program: Technical Program and Model Analytical Development," *Journal of Aircraft*, Vol. 37, No. 4, 2000, pp. 554–561. https://doi.org/10.2514/2.2654

[2] Zink, P. S., Mavris, D. N., and Raveh, D. E., "Maneuver Trim Optimization Techniques for Active Aeroelastic Wings," *Journal of Aircraft*, Vol. 38, No. 6, 2001, pp. 1139–1146. https://doi.org/10.2514/2.2884

[3] Eller, D., and Heinze, S., "A Computational Study on the Use of Redundant Control Surfaces to Improve the Induced Drag of Aeroelastic Configurations," Royal Inst. of Technology, Aeronautical and Vehicle Engineering TR, Stockholm, Sweden, 2003, https://www.diva-portal.org/smash/record.jsf?pid=diva2%3A321257=-7241.

[4] Weisshaar, T. A., and Duke, D. K., "Induced Drag Reduction Using Aeroelastic Tailoring with Adaptive Control Surfaces," *Journal of Aircraft*, Vol. 43, No. 1, 2006, pp. 157–164. https://doi.org/10.2514/1.12040

[5] Kolonay, R. M., and Eastep, F., "Optimal Scheduling of Control Surfaces Flexible Wings to Reduce Induced Drag," *Journal of Aircraft*, Vol. 43, No. 6, 2006, pp. 1655–1661. https://doi.org/10.2514/1.14604

[6] Zink, P. S., Love, M. H., and Youngren, H., "Drag Minimization Through the Use of Mission Adaptive Trailing Edge Flaps and Fuel State Control," *Collection of Technical Papers—10th AIAA/ISSMO Multidisciplinary Analysis and Optimization Conference*, Vol. 2, AIAA, Reston, VA, 2004, pp. 747–767; also AIAA Paper 2004-4365, 2004.

[7] Reich, G., Raveh, D., and Zink, P., "Application of Active-Aeroelastic-Wing Technology to a Joined-Wing Sensorcraft," *Journal of Aircraft*, Vol. 41, No. 3, 2004, pp. 594–602. https://doi.org/10.2514/1.78

[8] Yagil, L., Raveh, D. E., and Idan, M., "Deformation Control of Highly Flexible Aircraft in Trimmed Flight and Gust Encounter," *Journal of Aircraft*, Vol. 55, No. 2, 2018, pp. 829–840. https://doi.org/10.2514/1.C034353

[9] Cosin, R., Angelo, M., Catalano, F., and Bonemer De Salvi, F., "Mission Adaptive Wing Optimization with Wind Tunnel Hardware in the Loop," *13th AIAA/ISSMO Multidisciplinary Analysis Optimization Conference*, AIAA Paper 2010-9201, 2010.

[10] Boria, F., Stanford, B., Bowman, S., and Ifju, P., "Evolutionary Optimization of a Morphing Wing with Wind-Tunnel Hardware in the Loop," *AIAA Journal*, Vol. 47, No. 2, 2009, pp. 399–409. https://doi.org/10.2514/1.38941

[11] Suh, P., Chin, A., and Mavris, D., "Virtual Deformation Control of the X-56A Model with Simulated Fiber Optic Sensors," NASA TM-2014-216616, 2014.

[12] Pak, C., "Wing Shape Sensing from Measured Strain," *AIAA Journal*, Vol. 54, No. 3, 2016, pp. 1068–1077. https://doi.org/10.2514/1.J053986

[13] Gherlone, M., Cerracchio, P., and Mattone, M., "Shape Sensing Methods: Review and Experimental Comparison on a Wing-Shaped Plate," *Progress in Aerospace Sciences*, Vol. 99, May 2018, pp. 14–26. https://doi.org/10.1016/j.paerosci.2018.04.001

[14] Freydin, M., Keren-Rattner, M., Raveh, D. E., Kressel, I., Davidi, R., and Tur, M., "Fiber-Optics-Based Aeroelastic Shape Sensing," *AIAA Journal*, Vol. 57, No. 12, 2019, pp. 5094–5103. https://doi.org/10.2514/1.J057944

[15] Todd, M., Malsawma, L., Chang, C., and Johnson, G., "The Use of Fiber Bragg Grating Strain Sensors in Laboratory and Field Load Tests: Comparison to Conventional Resistive Strain Gages," Tech. Rept., U.S. Naval Research Lab., Washington, D.C., 1999.

[16] Nahom, T., Raveh, D. E., and Iovnovich, M., "Wind-Tunnel Study of the Autoregressive Moving-Average Flutter Prediction Method," *Journal of Aircraft*, Vol. 56, No. 4, 2019, pp. 1441–1454. https://doi.org/10.2514/1.C035203

[17] Garmendia, D. C., "A Multi-Disciplinary Conceptual Design Methodology for Assessing Control Authority on a Hybrid Wing Body Configuration," Ph.D. Thesis, Georgia Inst. of Technology, Atlanta, GA, 2015.

[18] Zhao, W., and Kapania, R. K., "Actuator Energy and Drag Minimization of a Blended-Wing-Body with Variable-Camber Continuous Trailing-Edge Flaps," *Engineering Optimization*, Vol. 52, No. 9, 2020, pp. 1561–1587. https://doi.org/10.1080/0305215X.2019.1660776

[19] Foss, G. C., and Haugse, E. D., "Using Modal Test Results to Develop Strain to Displacement Transformations," *Proceedings of the SPIE*, SPIE, Bellingham, WA, 1995, pp. 112–112.

[20] Avin, O., Raveh, D. E., Drachinsky, A., Ben-Shmuel, Y., and Tur, M., "Experimental Aeroelastic Benchmark of a Very Flexible Wing," *AIAA Journal*, Vol. 60, No. 3, 2022, pp. 1745–1768. https://doi.org/10.2514/1.J060621

[21] *MSC NASTRAN Quick Reference Guide*, MSC Software, Newport Beach, CA, 2014.

[22] *ZAERO User's Manual*, ZONA Technology, Scottsdale, AZ, 2013.

[23] Stanford, B. K., "Optimization of an Aeroservoelastic Wing with Distributed Multiple Control Surfaces," *Journal of Aircraft*, Vol. 53, No. 4, 2016, pp. 1131–1144. https://doi.org/10.2514/1.C033613

[24] Schmidt, O. T., and Colonius, T., "Guide to Spectral Proper Orthogonal Decomposition," *AIAA Journal*, Vol. 58, No. 3, 2020, pp. 1023–1033. https://doi.org/10.2514/1.J058809